Developing Geostationary Satellite Imaging at the Navy Precision Optical Interferometer

Dr. Gerard T. van Belle
Lowell Observatory, Flagstaff, AZ 86001

Abstract

The Navy Precision Optical Interferometer (NPOI) is a six-beam long-baseline optical interferometer, located in Flagstaff, Arizona; the facility is operated by a partnership between Lowell Observatory, the US Naval Observatory, and the Naval Research Laboratory. NPOI operates every night of the year (except holidays) in the visible with baselines between 8 and 100 meters (up to 432m is available), conducting programs of astronomical research and technology development for the partners. NPOI is the only such facility as yet to directly observe geostationary satellites, enabling milliarcsecond resolution of these objects. To enhance this capability towards true imaging of geosats, a program of facility upgrades will be outlined. These upgrades include AO-assisted large apertures feeding each beam line, new visible and near-infrared instrumentation on the back end, and infrastructure supporting baseline-wavelength bootstrapping which takes advantage of the spectral and morphological features of geosats. The large apertures will enable year-round observations of objects brighter than 10th magnitude in the near-IR. At its core, the system is enabled by a approach that tracks the low-resolution (and thus, high signal-to-noise), bright near-IR fringes between aperture pairs, allowing multi-aperture phasing for high-resolution visible light imaging. A complementary program of visible speckle and aperture masked imaging at Lowell's 4.3-m Discovery Channel Telescope, for constraining the low-spatial frequency imaging information, will also be outlined, including results from a pilot imaging study.

1 Current Status of NPOI

The Navy Precision Optical Interferometer (NPOI) is an operational long-baseline optical interferometer, combining up to six beams from independent telescopes. The current small (12-cm) apertures have been used for development of a high-precision astrometric catalog [1], world-first interferometric observations of geosats [2, 3], along with scientific investigations [4, 5, 6, 7]. Recent technical developments include a new six-way beam combiner [8], and a updated instrument back end that provides multi-baseline bootstrapping and coherent integration of fringe visibilities [9, 10]. A detailed instrument paper [11] and a recent update [12] are available.

2 Proposed Architecture

For an integrated solution to the challenge of imaging high-altitude ($\gtrsim$1,000 miles) satellites, including (but not limited to) geostationary satellites, we are leveraging two major, operational facilities for which Lowell Observatory has privileged access: the observatory's 4.3-m Discovery Channel Telescope (DCT), and NPOI. Both of these facilities are operating on-sky *right now* on a daily basis and constitute major infrastructure investments which can be immediately utilized to test and validate many of the techniques necessary for an operational geosat imaging facility.

The system architecture has the following high-level elements: (1) *Optical interferometry.* Spatial resolution in the sub-arcsecond to single-milliarcsecond regime requires an interferometric telescope array. Observing in the 'optical' – namely, both visible and near-infrared wavelengths – is required to both achieve the spatial resolution, but also to observe the features of interest on geosats.

(2) *Reconfigurable array.* Geosats range in spatial scale from 10-200-mas, so adjusting the resolving power of the array through reconfiguration is needed. Additionally, a reconfigurable array provides dense access to $\{u, v\}$ data points for image reconstruction. (3) *Baseline bootstrapping.* The desired resolution element size of 10-cm or smaller can be observed with the longest baselines of an interferometric array, but at low signal-to-noise-ratio (SNR); as such, tracking on short baselines with their high SNR is necessary to coherently lock the long baselines. (4) *Wavelength bootstrapping.* Near-IR fringe tracking (FTK) has two significant (and essential) benefits: first, satellites are brighter in the near-IR than in the visible; second, the lower resolving power of longer wavelength observing means higher SNR for FTK. Both of these benefits increase the ability of an array to be coherently phased on a satellite for integrating ('staring') at visible wavelengths. (5) *Large apertures.* Satellites are faint relative to the current state-of-the-art in optical interferometry; adaptive-optics (AO) corrected apertures of size $\geq$1.0-m are required. (6) *Complementary single-aperture imaging.* Using the technique of non-redundant aperture masking (NRM), Lowell's 4.3-m DCT effectively can operate as a very-short-baseline optical interferometer and serve to constrain image reconstructions. Of these elements, items 1-3 and 6 have already advanced to on-sky operations.

The NPOI facility has the necessary flexibility for this task of high-altitude satellite imaging and could be optimized in the following ways:

- *Increased aperture size.* The current small 12-cm size of the individual feed apertures is poised to be completely overhauled with the installation of fixed 1.8-m telescopes. Four of these 1.8-m telescopes were built for the Keck Interferometer [13] but not installed for non-technical reasons; they were gifted to USNO in 2010 for installation at NPOI [14, 15] and a FY14 start for this project has been funded.

  Additionally, we have at least two options for additional large, moveable apertures. The first option is lightweight 1.4-m carbon-fiber reinforced-polymer telescopes [CFRP, 16] that have been undergoing development for use at NPOI. These lightweight ($\approx$ 100 kg) telescopes are optimized for flexible relocation to NPOI imaging stations, augmenting the fixed 1.8-m apertures. The second option will be more 'traditional' 1.0-m telescopes based upon lightweighted fused silica glass mirrors, readily available commercially.

- *Adaptive optics.* Turnkey adaptive optics systems are now available commercially. Both natural- and laser-guide-star systems are robust, operating reliably and rapidly [17].

- *Short baseline stations.* NPOI has stations with separations down to $\sim$3 m at the center of the array, though with the complementary use of NRM at the DCT, spacings only at the $\sim$8 m level are needed. Our currently operational stations allow for long baselines to be constructed out of short spacings; additional stations could be commissioned, optimized for the satellite observing case.

- *Baseline bootstrapping.* A paradox of imaging with interferometry is that short baselines are needed to produce fringe visibilities significant enough to track, but long baselines, where fringes are too weak to track, are needed for high resolution imaging. The NPOI is designed to resolve this paradox by building medium to long baselines from a chain of shorter baselines, using the technique of baseline bootstrapping.

- *Wavelength bootstrapping.* Satellites are significantly brighter at near-infrared wavelengths; typical $V - J$ and $V - H$ colors are 2.75 & 3.25 [18]. A second benefit in the near-infrared is that, at longer wavelengths, fringe contrast increases. A useful technique is to cophase the array at a high SNR wavelength – in this case, the near-IR – but then take advantage of the cophased array and do imaging at a second, lower SNR wavelength – in this case, the visible. Two benefits come from this approach. First, the material constituting the spacecraft bus are brighter relative to the solar panels in the visible; second, the shorter wavelength for imaging should provide greater spatial resolution.

The long-baseline interferometry of NPOI is neatly complemented by short-baseline interferometry with the DCT (next section).

3 Speckle Imaging & Non-Redundant Aperture Masking

One of the primary examples commonly cited in desired SSA of geosats, namely "confirming the successful deployment of solar panels", is already readily achievable through use of amplitude interferometry on a large ($>$ 4-m) single-aperture telescope. Recent pilot speckle interferometry observations carried out in 2014 at the DCT have already demonstrated exactly this capability. Using the Differential Speckle Survey Instrument [DSSI, 19], we observed a variety of geosats and other high-altitude satellites with simultaneous operational wavelengths of 692-nm & 880-nm, resulting in resolving power of 33-mas & 42-mas (the reconstructions from the former are seen in Fig. 1); this is $\approx$ 7 pixels across large geosats (roughly 6-m resolution). Although this does not seem like terribly fine resolution, it is indeed sufficient to establish the status of the solar panel deployment on these geosats - not too shabby for an instrument that had a capital investment of $\approx$\$200k for construction from off-the-shelf components.

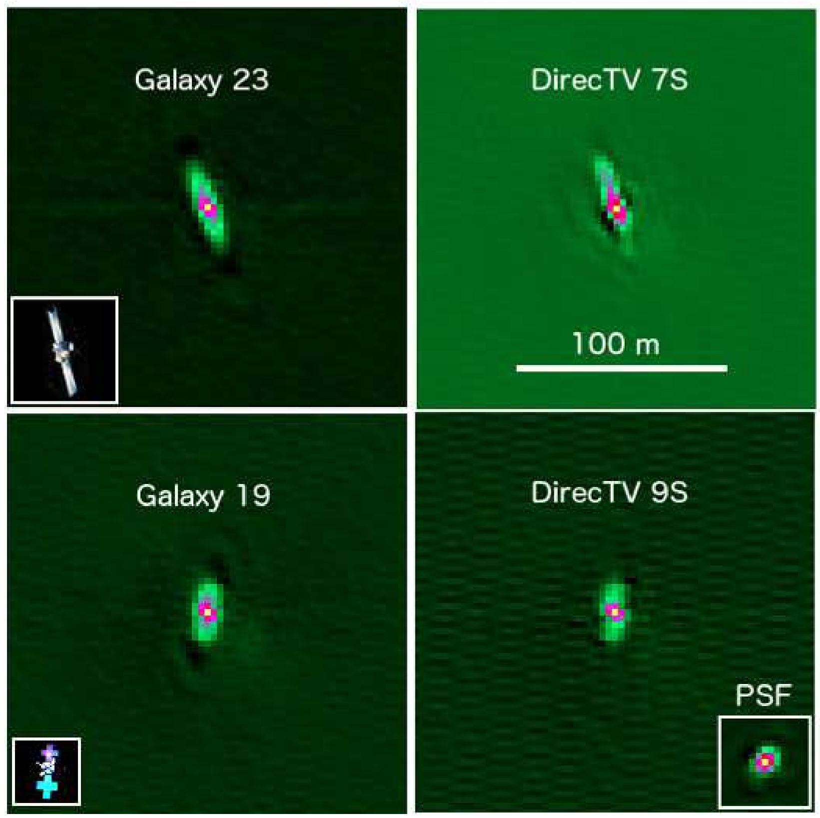

Fig. 1: A montage of speckle images of geosats taken with DSSI@DCT. Galaxy-23, DirecTV-7S, and -9S are all based upon the LS-1300 satellite bus with long, straight solar panels (see upper left inset); Galaxy-19 is also a LS-1300 but with an '+' configuration for its solar panels (lower left inset panel). We surmise DirecTV-9S's foreshortened appearance is due to it being an on-orbit spare, and is tilted relative towards the sun (and our line of sight) to reduce its weathering. The point-spread-function of DSSI is seen in the lower right inset panel.

Furthermore, this same instrument is actually quite short of its full potential in this demonstration. Operational wavelengths include filters at 325-nm & 370-nm, resulting in a factor of $\sim 2\times$ better than operations at the longer wavelengths. The sensitivity limit for DSSI is $V \approx 14$ on the DCT; secondary objects relative to primaries of this brightness can be detected with a brightness

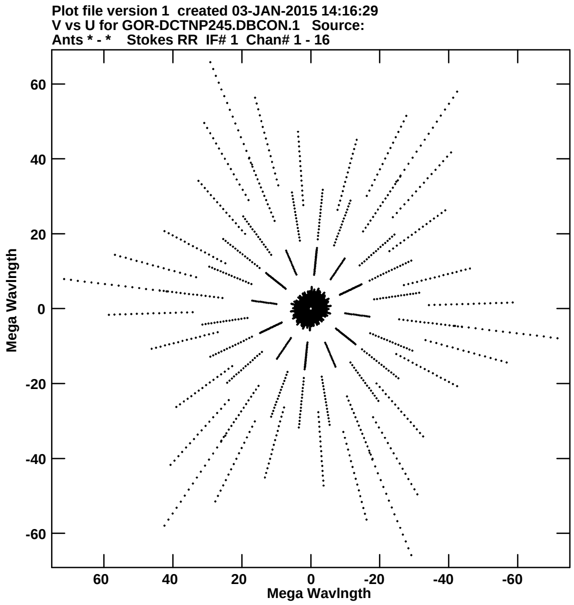

Fig. 2: The $\{u, v\}$ plane coverage of combined DCT and NPOI observations. The central core of data points are the DCT NRM points, with the radial 'spikes' of coverage coming from NPOI employing its core short-baseline stations, numbers 2-4-5 for the north, east, and west arms.

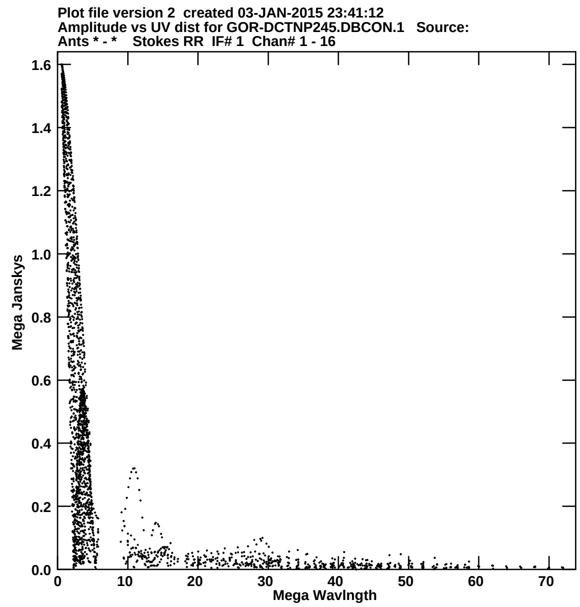

Fig. 3: The expected visibilities from combined DCT and NPOI observations. As with Fig. 2, the central core at low spatial frequencies corresponds to the DCT NRM data, with the high frequency data coming from NPOI.

difference of $\Delta M = 3.5$ at separations of 200-mas [20].

The closely related technique of non-redundant aperture masking (NRM) on a single telescope is the logical extension of the speckle technique, potentially with improvements in the available contrast ratios over basic speckle interferometry. NRM has been demonstrated on the 8.2-m VLT UT4 telescope as a robust and efficient method for detection of faint stellar companions, and as an approach that improves the effective resolving power of a single aperture from $1.22\lambda/D$ to $\lambda/2D$ [21].

Timeliness of speckle imaging or NRM is related to the operational model of the facility. Given Lowell Observatory's ownership and direct control over the 4.3-m DCT, significantly more nimble response time is available. The DCT is scheduled on a quarterly basis, and schedule-interrupt arrangements can be made ahead of time for even quicker turnaround if necessary. As an extreme example, the University of Maryland has an agreement with Lowell Observatory to task the DCT on only 15 minutes notice, for capturing follow-up observations of gamma-ray bursters. Observing of this nature typically completes an imaging data cube in a few minutes.

4 Interferometry

4.1 Interferometry Primer

The images of geosats from Lowell's 4.3 m Discovery Channel Telescope (Fig. 1), with $\approx$ 6 m resolution at red visual wavelengths, and those from the 10 m Keck II Telescope [22], with ≈ 5 m resolution at 1.3 μm, demonstrate that apertures much larger than 10 m are needed in order to make detailed images of these targets.

An interferometer can overcome these resolution limits by combining light from two or more telescopes to form a virtual aperture with a diameter equal to the separation between telescopes. The relay optics are adjusted so that the difference ΔD between the path lengths from the target through each of the telescopes to the beam combiner, is 0, ideally within a wavelength.

Depending on the length and orientation of the telescope separations and on the target's size, the interference formed by the light from each pair of telescopes can range from strong to nonexistent; and depending on the target's shape and on the positions of its features, we may see the path difference ΔD at which maximum interference takes place shift away from 0.

The data from the interferometer consists of the strength, or "visibility" V, of the interference and its phase $\delta\phi$ ($= \Delta D/\lambda$, where λ is the observing wavelength), both as a function of the baseline $\mathbf{B}$, the vector separation of each pair of telescopes. The magnitude of V ranges from 0 (no interference) to 1 (strong interference). Typically, we take data in many wavelength channels simultaneously, so V is a function of λ as well. From these visibility data, $V(\mathbf{B}, \lambda) \exp i\phi(\mathbf{B}, \lambda)$, we reconstruct the image of the target.

However, the process of combining the beams with the required precision and making detailed images faces a number of challenges. One such challenge is posed by atmospheric turbulence, which significantly changes the effective path lengths through the atmosphere on $\sim$ 10 ms timescales. Interferometers use the visibility data to measure this effect, and then counteract it by adjusting the relay optics. This adjustment requires that the signal-to-noise ratio $NV^2/2 \gtrsim 1$, where N is the number of photons detected within the 10 ms atmospheric timescale. The atmospheric timescale is the dominant effect limiting the sensitivity of the interferometer.

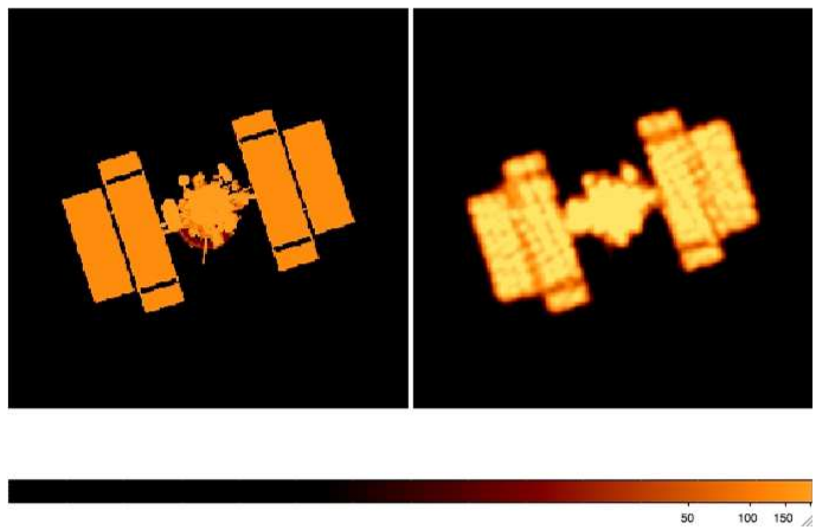

Fig. 4: A simulation of true (left) versus reconstructed image of a Gorizont geosat using the DCT-NPOI $\{u, v\}$ plane coverage seen in Fig. 2. The pixel size is 0.476-mas and the image size is 256 pixel ($\sim$122-mas).

Requiring $NV^2/2 \gtrsim 1$ to correct for the effects of turbulence means that we need the visibility $|V|$ to be greater than a few $\times 0.1$ for typical values of N. However, for typical target images, this requirement is met only on short, low-resolution baselines, as Fig. 3 demonstrates. In this figure, which shows visibility amplitudes as a function of baseline length in simulated observations of a Gorizont geosat in the 550 nm to 850 nm wavelength range (Fig. 4), $|V|$ is high enough to use for these corrections only on baselines shorter than $\sim$ 10 m to 20 m. But it is the information on the long baselines that is needed to image the details of the target. This is a second challenge for optical interferometry: how do we stabilize the interferometer in order to obtain high-resolution data?

The solution to this problem is twofold: observe at longer wavelengths, and lay out the array with chains of telescopes. At longer wavelengths, such as the J- ($1.1 - 1.4$ μm), H- ($1.4 - 1.8$ μm), or K- ($2.0 - 2.4$ μm) bands, the baselines can be two to three times longer before the target is over-resolved. Correcting the atmospherically induced path length variations using these infrared bands also corrects them at the visual wavelengths on these longer, higher-resolution baselines, a technique known as "wavelength bootstrapping."

We can also perform a second kind of bootstrapping by using a chain of telescopes. If we use a row of three telescopes with, e.g., 25-m spacing observing in the J-band, stabilizing the 25-m baselines between the first and second and between the second and third telescopes automatically stabilizes the 50-m baseline between the first and third telescopes, allowing us to take data on that baseline even though NV^2 on that baseline is too low to directly detect fringes. This "baseline bootstrapping" technique can also be extended to longer chains.

The final challenge is to obtain data over a wide enough range of baseline lengths and orientations to produce a reliable image, also known as "$\{u, v\}$ coverage" (Fig. 2). In astronomical interferometry, we rely on the rotation of the Earth to change the baseline orientations, so a Y-shaped configuration with several telescopes along each arm, such as those at the NPOI or at CHARA, is sufficient. For geosat observations, Earth rotation does not help, so an array dedicated to satellite observations requires a configuration that provides more baseline orientations.

4.2 Baseline-Wavelength Bootstrapping

Given their potential for high-resolution imaging, long-baseline optical interferometers (LBOI) have long been considered leading candidates for satisfying the requirements for Space Domain Awareness. In particular, the sub-milliarcsecond ($\lesssim$ 10nrad) resolution requirement dictates an optical system with a gross size of at least 40m, in excess of even the most ambitious single-aperture telescope projects currently envisioned.

As introduced in the previous section, the combination of baseline and wavelength bootstrapping can be combined into 'baseline-wavelength bootstrapping'. This combination allows high-resolution observations of extended objects using LBOI. The baseline bootstrapping aspect of this technique has already been demonstrated, at NPOI and two other facilities (CHARA, VLTI).

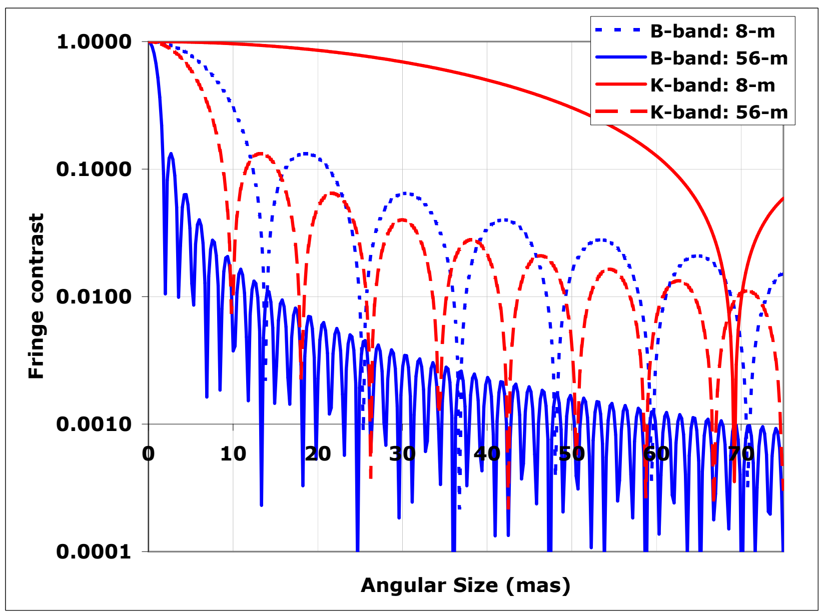

Fig. 5: Visibilities expected from objects of increasing gross size, as a function of wavelength and bootstrapping versus imaging baseline (8m / 56m). As a rough rule-of-thumb, K-band fringe contrast at the ∼5-10% level dictates the maximum gross projected size of the object for fringe tracking purposes (∼60mas); the number of B-band fringe contrast 'bumps' inside that envelope correspond roughly to the number of imaging resolution elements (∼40).

However, a criticism that has been leveled against bootstrapping is the claim that it will not scale well to targets that are heavily resolved, i.e., those targets whose angular size, θ_0, is many times the desired resolution, $\theta_{\rm min}$, of the longest baseline. The root of the claim is that the ratio of the longest baseline to the short baselines used for bootstrapping, $B_{\rm max}/B_{\rm boot}$, must be $\simeq \theta_0/\theta_{\rm min}$ because the short baselines must be short enough to produce trackable fringes from the large-scale structure of the target, while the longest baselines must resolve small-scale structure at the desired high resolution. Thus if 25cm resolution is desired on a 10m target, $B_{\rm max}/B_{\rm boot} \simeq 40$. This criticism claims that the accumulation of phase errors across 40 steps of bootstrapping will render the technique unworkable.

This critique is invalid for systems that satisfy the parameters of geosat imaging because it overlooks three factors that make baseline-wavelength bootstrapping such a practical, powerful combination. First, wavelength bootstrapping from infrared to visible wavelengths can increase $B_{\rm boot}$ by factors from 3 to 6. Wavelength bootstrapping entails tracking fringes in the infrared H- (1.6μm) or K- (2.2μm) bands in order to stabilize the fringes in the visual bands (0.4 to 1.0μm). Because resolution scales inversely with wavelength, $B_{\rm boot}$ at K-band can be $\simeq$5 times longer than $B_{\rm boot}$ at 0.4μm, reducing the number of bootstrapping effects by the same factor. Fig. 5 illustrates the concept: with $B_{\rm boot} = 8$m observing at K band (solid red line), the fringe contrast for a $\theta_0 = 40$mas (= 200nrad = 7m at GEO) target is $V \simeq 0.5$. Bootstrapping eight stations together, (i.e. $B_{\rm max} = 56$m) and observing at 0.4μm produces $V = 0.4$ fringes at resolution $\theta_{\rm min} = 1$mas (= 5nrad = 17cm at GEO). While the fringe-tracking SNR requirements significantly increase with long-wavelength bootstrapping for short-wavelength imaging, we will show in the next section that these are not insurmountable.

Second, we take advantage of the fact that geosats are significantly brighter in the near IR than at visible wavelengths [$m_V - m_K \simeq 3$; 18].

Third, geosatellite targets have more small-scale structure than the uniform-disk targets implicitly invoked in the critique. The target used in this estimate of this section is a uniform disk, the worst-case scenario. Because these targets are more complex, they produce higher visibility fringes at a given resolution than would a uniform disk with the same overall size (Fig. 6). The result is that the short bootstrapping baselines $B_{\rm boot}$ can be longer than the length $B = \lambda/\theta_0$ that the critique would claim.

A baseline-wavelength bootstrapping demonstration is readily possible with NPOI. An additional, *necessary* benefit of bootstrapping is that image information from baselines that are short, long, and all lengths in-between is captured, allowing for non-aliased image reconstruction; avoiding baseline bootstrapping fundamentally limits the ability to reconstruct images, due to the missing mid-length baselines.

4.3 Sensitivity Limit: Fringe Tracking and Adaptive Optics

The tracking of interference fringes is at the heart of any interferometric system, particularly one peering through the Earth's turbulent atmosphere, so a detailed examination of the performance of such a technique is warranted. For an on-sky source of magnitude m_λ, the number of detected photons per integration frame per aperture is:

$$N_1 = F_{\lambda,0} 10^{-m_\lambda/2.5} \pi (D_1/2)^2 t_0 V_{\rm obj}^2 T Q (\Delta\lambda/\lambda_c)/s_1 \tag{1}$$

where $F_{\lambda,0}$ is the source flux for a zero-magnitude star at the bandpass λ; D_1 is the diameter of aperture 1; t_0 is the integration time; $V_{\rm obj}^2$ is the object visibility; T is the throughput to the detector; Q is the detector quantum efficiency; $\Delta\lambda/\lambda_c$ is the fractional bandpass for the band in question; and s_1 is the number of beam splits for recombination, which in the case of pairwise combination (for nearest-neighbor fringe tracking) is 2. A similar calculation for the second aperture produces a value for N_2. The integration time t_0 is matched to the expected coherence time for the observational wavelength; in the case of V-band observations, t_0 is expected to be (on reasonable nights) 5ms, and scales as $\lambda^{6/5}$.

The relevant noise has 3 sources: thermal, sky, and read noise. The detected thermal background photons per integration frame per aperture, B_T, and sky background S can be computed as well:

$$B_T = t_0 Qe(\Delta\lambda/\lambda_c)P, \text{ with } P = \frac{2hc^2}{\lambda^5}\frac{1}{e^{hc/\lambda k_B T} - 1}; \quad S = t_0 Qe(\Delta\lambda/\lambda_c)TA \tag{2}$$

where e is the entendue (simply 1 in this case), and P is the familiar Planck function, including the Planck constant h, Boltzmann constant k_B, ambient temperature T, and speed of light c; A is the air glow rate: for V, J, H, K bands, respectively, is 0, 910, 9700 and 14000 counts/frame. Additionally the count rate due to read noise is $R = 4 \times \mathrm{rn}^2$. Thus, the total noise N_n and signal-to-noise SNR are

$$N_n = \sqrt{N_1 + \frac{B_T + S}{s_1} + N_2 + \frac{B_T + S}{s_2} + R}, \qquad SNR = \frac{4}{\pi}\frac{\sqrt{2N_1N_2\sqrt{\mathrm{St}_1\mathrm{St}_2}}}{N_n} \tag{3}$$

where St_x is the Strehl ratio for aperture x; the Strehl is a measurement of the goodness of wavefront quality for a given aperture, ranging from 0 (fully aberrated) up to 1 (unaberrated), scaling roughly as the rms deviation σ of the wavefront phase over the aperture ($\sigma^2 =< (\phi - \overline{\phi})^2 >$), $St \approx e^{-\sigma^2}$ [23, 24]. We adopt here the published performance numbers of the Robo-AO laser-guide-star adaptive optics (LGS-AO) system [17] as an existence proof of turnkey LGS-AO; namely St=26% at 762nm, LGS wavelength of 355nm, a limiting magnitude of $m_V < 16$ and highly efficient operations (<1 minute acquisition time). As with coherence time, the Strehl ratio is expected to scale as $\lambda^{6/5}$, for St_B=14% and St_K=93% at $B-$ and $K-$band, respectively.

Read noise numbers are set to performance seen in the visible for detector systems commonly available (both avalanche photo diodes and electron-multiplying CCD cameras), which are quite good (1e-); in the near-infrared, the First Light Instruments SELEX Saphira camera is baselined, with its notable near-IR performance (3e- single correlated double read).

For a given SNR target, we can solve Equations 1 through 3 for m_λ to establish a limiting astronomical magnitude, accounting for detector performance issues (particularly read noise), background (which becomes an issue only at K-band), atmosphere (including single-aperture Strehl ratio and integration time).

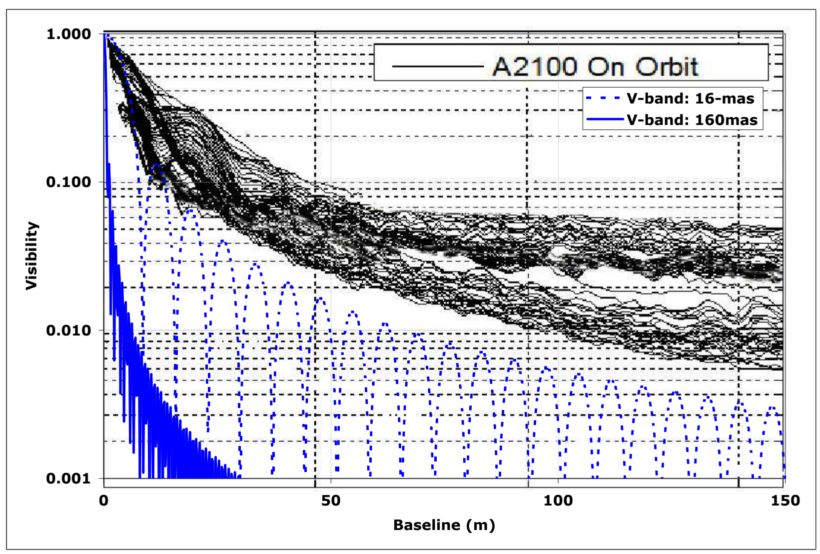

Fig. 6: Visibilities as a function of baseline length at 550nm generated from an A2100 satellite model (black), along with uniform disks of sizes consistent with the major and minor axis sizes of an A2100 (blue).

We set that SNR target to 3 when considering our long imaging baseline; this in turn sets the fringe-tracking SNR, which has to increase upwards due to two factors. First, fringe tracking errors scale linearly with λ [25]; for going from B-band to K-band, this corresponds to a factor of 4.9×. Second, the same errors accumulate as the square root of the number of baselines ($\sqrt{N}$), which corresponds to factors of 2.45× and 2.83× for 6- and 8-way systems, respectively.

Given this computational framework, we can compute the limiting magnitudes for two architectures: a notional 8 $\times$ 1.5-m aperture LBOI, and the current 6 $\times$ 12cm NPOI (Table 1), for the cases of K-band fringe tracking, as well as B-band stabilized fringe integration cases with long synthetic coherence times ($\sim$1.5 sec), on a 60mas target with 8m short baseline spacing. As seen in the final line of Table 1, a limiting magnitude of our notional 8-way large-aperture architecture is m_K=8.7, which corresponds to $m_V \simeq 11.7$ given the very red satellite colors noted above; this limit also agrees well with the m_B limit also presented in the table.

5 Summary

Demonstration of the key high-altitude satellite imaging technologies would be possible through the simple addition of near-IR fringe-tracking hardware to the existing infrastructure of the 6-aperture NPOI, with its sensitivity limits for stellar test sources noted in Table 1. In particular, NPOI is uniquely positioned for immediate demonstration of the necessary system engineering, integration & test, and on-sky demo of the baseline-wavelength bootstrapping technique with $N > 4$ apertures. Further significant retirement of system implementation risk could be achieved through demonstrating integration of 1.5m LGS-AO apertures at the NPOI facility. Specifically, direct demonstration of the accumulation of errors in the baseline-wavelength bootstrapping system for both wavelength-dependent phenomena (e.g. atmospheric DCR), independent phenomena (e.g. telescope motion), and other terms (e.g. influence of Strehl ratio) would guide design & implementation of a final operational system.

It is also worth noting the scalability of this architecture: a notional 12 $\times$ 1.5m system would still have a limiting sensitivity of $m_K = 8.0$ (corresponding to $m_V = 11.0$), with a resolution of 8.9cm. Ultimately, using this approach it appears that the accumulated fringe-tracking errors degrades this architecture to a $m_V = 10.0$ specification at around 32 $\times$ 1.5m apertures (with $\sim$3.2cm resolution at 35,000km). Gaining a magnitude of sensitivity is possible with N-way systems by going to 2.3m apertures.

Table 1: Expected performance of systems with pairwise K-band fringe tracking for N-way B-band imaging: either 8 $\times$ 1.5m apertures for a notional testbed, or 6 $\times$0.12m for NPOI; the short K-band baselines in each case are 8m in length.

Parameter	**Units**	**8-way $\times$ 1.5m**		**NPOI**		**Notes**
		K-band	**B-band**	**K-band**	**B-band**	
Wavelength	um	2.22	0.44	2.22	0.44	
Aperture size	m	1.50	1.50	0.12	0.12	
Aperture strehl		0.93	0.14	0.95	0.40	
Splits		2	8	2	6	
Integration time	sec	0.040	1.500	0.040	1.500	
Read noise	e rms	3	1	3	1	As appropriate for detector system
Optics temperature	K	290	290	290	290	Ambient room temperature
Optics emissivity		0.46	0.46	0.46	0.46	After 20 reflections at 0.97
Baseline	m	8	56	8	40	$(N_{\mathrm{TEL}} - 1) \times$ 8m for imaging
Object V^2		0.12	0.0013	0.12	0.0021	For 60mas projected size
Throughput to detector		0.54	0.54	0.54	0.54	20 reflections at 0.97
Detector QE		0.7	0.7	0.7	0.7	
Resolution	cm		14.1		19.7	At 35,000 km
SNR		41.6	3.0	36.0	3.0	
Magnitude Limit		8.7	11.8	3.5	8.4	

References

[1] J. A. Benson, D. J. Hutter, R. T. Zavala, H. C. Harris, P. D. Shankland, and K. J. Johnston. From fringes to the USNO Navy Prototype Optical Interferometer Astrometric Catalog. In *Society of Photo-Optical Instrumentation Engineers (SPIE) Conference Series*, volume 7734 of *Society of Photo-Optical Instrumentation Engineers (SPIE) Conference Series*, page 3, July 2010.

[2] J. T. Armstrong, R. B. Hindsley, H. R. Schmitt, F. J. Vrba, J. A. Benson, D. J. Hutter, and R. T. Zavala. Detection of a geostationary satellite with the Navy Prototype Optical Interferometer. In *Society of Photo-Optical Instrumentation Engineers (SPIE) Conference Series*, volume 7734 of *Society of Photo-Optical Instrumentation Engineers (SPIE) Conference Series*, July 2010.

[3] R. B. Hindsley, J. T. Armstrong, H. R. Schmitt, J. R. Andrews, S. R. Restaino, C. C. Wilcox, J. A. Benson, F. J. Vrba, M. E. DiVittorio, D. J. Hutter, P. D. Shankland, R. T. Zavala, and S. A. Gregory. *Applied Optics*, 50:2692, 2012.

[4] R. T. Zavala, S. J. Adelman, C. A. Hummel, A. F. Gulliver, H. Caliskan, J. T. Armstrong, D. J. Hutter, K. J. Johnston, and T. A. Pauls. The Mercury-Manganese Binary Star phi Herculis: Detection and Properties of the Secondary and Revision of the Elemental Abundances of the Primary. ApJ, 655:1046–1057, February 2007.

[5] M. Hillen, T. Verhoelst, H. Van Winckel, O. Chesneau, C. A. Hummel, J. D. Monnier, C. Farrington, C. Tycner, D. Mourard, T. ten Brummelaar, D. P. K. Banerjee, and R. T. Zavala. An interferometric study of the post-AGB binary 89 Herculis. I. Spatially resolving the continuum circumstellar environment at optical and near-IR wavelengths with the VLTI, NPOI, IOTA, PTI, and the CHARA Array. A&A, 559:A111, November 2013.

[6] E. K. Baines, J. T. Armstrong, H. R. Schmitt, J. A. Benson, R. T. Zavala, and G. T. van Belle. Navy Precision Optical Interferometer Measurements of 10 Stellar Oscillators. ApJ, 781:90, February 2014.

[7] B. Kloppenborg, R. Stencel, J. D. Monnier, G. Schaefer, F. Baron, C. Tycner, R. T. Zavala, D. Hutter, M. Zhao, X. Che, T. ten Brummelaar, C. Farrington, R. Parks, H. McAlister, J. Sturmann, L. Sturmann, P. J. Sallave-Goldfinger, N. Turner, E. Pedretti, and N. Thureau. Interferometry of ϵ Aurigae: Characterization of the asymmetric eclipsing disk. *ArXiv e-prints*, August 2015.

[8] A. Ghasempour, M. W. Muterspaugh, D. J. Hutter, J. D. Monnier, J. A. Benson, J. T. Armstrong, M. H. Williamson, S. Fall, C. Harrison, and C. Sergeyous. Building the next-generation science camera for the Navy Optical Interferometer. In *Society of Photo-Optical Instrumentation Engineers (SPIE) Conference Series*, volume 8445 of *Society of Photo-Optical Instrumentation Engineers (SPIE) Conference Series*, page 0, July 2012.

[9] A. M. Jorgensen, D. Mozurkewich, H. R. Schmitt, G. T. van Belle, D. J. Hutter, J. Clark, J. T. Armstrong, E. K. Baines, K. Newman, M. Landavazo, B. Sun, and S. R. Restaino. Progress toward unprecedented imaging of stellar surfaces with the Navy precision optical interferometer. In *Society of Photo-Optical Instrumentation Engineers (SPIE) Conference Series*, volume 9146 of *Society of Photo-Optical Instrumentation Engineers (SPIE) Conference Series*, page 0, July 2014.

[10] J. T. Armstrong, A. M. Jorgensen, H. R. Neilson, D. Mozurkewich, E. K. Baines, and H. R. Schmitt. Precise stellar diameters from coherently averaged visibilities. In *Society of Photo-Optical Instrumentation Engineers (SPIE) Conference Series*, volume 8445 of *Society of Photo-Optical Instrumentation Engineers (SPIE) Conference Series*, page 3, July 2012.

[11] J. T. Armstrong, D. Mozurkewich, L. J. Rickard, D. J. Hutter, J. A. Benson, P. F. Bowers, N. M. Elias, II, C. A. Hummel, K. J. Johnston, D. F. Buscher, J. H. Clark, III, L. Ha, L.-C. Ling, N. M. White, and R. S. Simon. The Navy Prototype Optical Interferometer. ApJ, 496:550, March 1998.

[12] J. T. Armstrong, D. J. Hutter, E. K. Baines, J. A. Benson, R. M. Bevilacqua, T. Buschmann, J. H. Clark, A. Ghasempour, J. C. Hall, R. B. Hindsley, K. J. Johnston, A. M. Jorgensen, D. Mozurkewich, M. W. Muterspaugh, S. R. Restaino, P. D. Shankland, H. R. Schmitt, C. Tycner, G. T. van Belle, and R. T. Zavala. The Navy Precision Optical Interferometer (npoi): AN Update. *Journal of Astronomical Instrumentation*, 2:40002, December 2013.

[13] J. Bell, J. M. Walker, P. L. Wizinowich, K. Tsubota, A. C. Rudeen, D. McBride, K. K. Kinoshita, M. Hrynevych, P. Goude, M. M. Colavita, J. H. Kelley, G. T. van Belle, R. Brunswick, J. K. Little, and C. H. Smith. Outrigger telescopes for narrow-angle astrometry. In J. M. Oschmann, Jr., editor, *Ground-based Telescopes*, volume 5489 of *Society of Photo-Optical Instrumentation Engineers (SPIE) Conference Series*, pages 962–973, October 2004.

[14] M. DiVittorio, D. J. Hutter, and M. Kelley. Plans for utilizing the Keck Outrigger Telescopes at NPOI. In *Society of Photo-Optical Instrumentation Engineers (SPIE) Conference Series*, volume 7013 of *Society of Photo-Optical Instrumentation Engineers (SPIE) Conference Series*, July 2008.

[15] P. D. Shankland, M. E. DiVittorio, D. J. Hutter, J. A. Benson, R. T. Zavala, and K. J. Johnston. The Science with Four 1.8-m Telescopes at the Navy Prototype Optical Interferometer. In *American Astronomical Society Meeting Abstracts #215*, volume 42 of *Bulletin of the American Astronomical Society*, page #441.12, January 2010.

[16] J. Andrews, T. Martinez, S. Restaino, F. Santiago, C. Wilcox, S. Teare, R. Romeo, and R. Martin. Carbon Fiber Reinforced Polymer (CFRP) Optics Quality Assessment for Lightweight Deployable Optics. In *Advanced Maui Optical and Space Surveillance Technologies Conference*, September 2010.

[17] C. Baranec, R. Riddle, N. M. Law, A. N. Ramaprakash, S. Tendulkar, K. Hogstrom, K. Bui, M. Burse, P. Chordia, H. Das, R. Dekany, S. Kulkarni, and S. Punnadi. High-efficiency Autonomous Laser Adaptive Optics. ApJ, 790:L8, July 2014.

[18] D. J. Sanchez, S. A. Gregory, D. Werling, T. E. Payne, L. Kann, L. G. Finkner, D. M. Payne, and C. Davis. Photometric measurements of deep space satellites. In J. W. Bilbro, J. B. Breckinridge, R. A. Carreras, S. R. Czyzak, M. J. Eckart, R. D. Fiete, and P. S. Idell, editors, *Imaging Technology and Telescopes*, volume 4091 of *Society of Photo-Optical Instrumentation Engineers (SPIE) Conference Series*, pages 164–182, October 2000.

[19] E. P. Horch, D. R. Veillette, R. Baena Gallé, S. C. Shah, G. V. O'Rielly, and W. F. van Altena. Observations of Binary Stars with the Differential Speckle Survey Instrument. I. Instrument Description and First Results. AJ, 137:5057–5067, June 2009.

[20] E. P. Horch, L. A. P. Bahi, J. R. Gaulin, S. B. Howell, W. H. Sherry, R. Baena Gallé, and W. F. van Altena. Speckle Observations of Binary Stars with the WIYN Telescope. VII. Measures during 2008-2009. AJ, 143:10, January 2012.

[21] S. Lacour, P. Tuthill, M. Ireland, P. Amico, and J. Girard. Sparse Aperture Masking on Paranal. *The Messenger*, 146:18–23, December 2011.

[22] J. D. Drummond and R. H. Rast. First Resolved Images of a Spacecraft in Geostationary Orbit with the Keck-II 10 m Telescope. In *The Advanced Maui Optical and Space Surveillance Technologies Conference*, 2010.

[23] K. Strehl. Über Luftschlieren und Zonenfehler. *Zeitschrift fr Instrumentenkunde*, 22:213–217, July 1902.

[24] V. N. Mahajan. Strehl ratio for primary aberrations in terms of their aberration variance. *Journal of the Optical Society of America (1917-1983)*, 73:860, 1983.

[25] A. Glindemann. *Principles of Stellar Interferometry*. Springer-Verlag, 2011.